Zhao *et al. Biochar* (2025) 7:24
https://doi.org/10.1007/s42773-024-00416-0

Biochar

ORIGINAL RESEARCH Open Access

Collaborative modification strategy to improve the formation of biochar-derived persistent free radicals for aniline removal via peroxymonosulfate activation

Zilong Zhao[1,2*], Shuting Zhu[1], Shuyu Qi[1], Ting Zhou[1], Yang Yang[1], Feng Wang[1], Qi Han[1], Wenyi Dong[1,3,4,5], Hongjie Wang[1,3,4,5] and Feiyun Sun[1]

Abstract

This study explores a novel approach to biochar modification aimed at increasing persistent free radical (PFR) formation on biochar surfaces, thereby enhancing aniline removal via peroxymonosulfate (PMS) activation. By adjusting pyrolysis temperatures and doping ratios, optimal conditions were established. Spearman's analysis highlighted the importance of C=C bonds, the I_D/I_G ratio, and pyridinic N in generating PFRs. The modified biochar derived at 500 ℃ (MB500), in conjunction with the PMS system demonstrated impressive efficiency, achieving 92% aniline removal within 30 min. Detailed adsorption tests and active species detection indicated that aniline degradation occurred through both direct oxidation by PFRs and indirect oxidation by reactive species, particularly superoxide radicals ($O_2{\cdot}^-$). Furthermore, the synergistic effects of heteroatom nitrogen and Na_2CO_3 modifications significantly impacted PFR formation and stability. These findings provide valuable insights into the mechanisms of PFR-mediated catalytic oxidation, highlighting the key roles of pyridinic rings, with or without oxygenated groups, in enhancing catalytic performance of biochar. This research advances the understanding of biochar surface chemistry and presents an effective strategy for developing high-performance biochar-based catalysts for environmental remediation, addressing the limitations of unmodified biochar through targeted surface modifications.

Highlights

- Heteroatom N and Na_2CO_3 modifications synergistically affect the PFRs formation on biochar.
- Pyridinic ring, with or without oxygenated groups, was the main sources of PFRs.
- PFRs-mediated catalytic oxidation dominated aniline degradation.
- $SO_4^{\cdot-}$ and $O_2^{\cdot-}$ generation significantly depends on PFRs concentration.
- Both $O_2{\cdot}^-$ radicals and $^1O_2$ non-radicals contributed to aniline degradation.

Keywords Persistent free radicals, Biochar, Synergistic modification, Peroxymonosulfate, Aniline degradation

*Correspondence:
Zilong Zhao
berthillon@hotmail.com
Full list of author information is available at the end of the article

Graphical Abstract

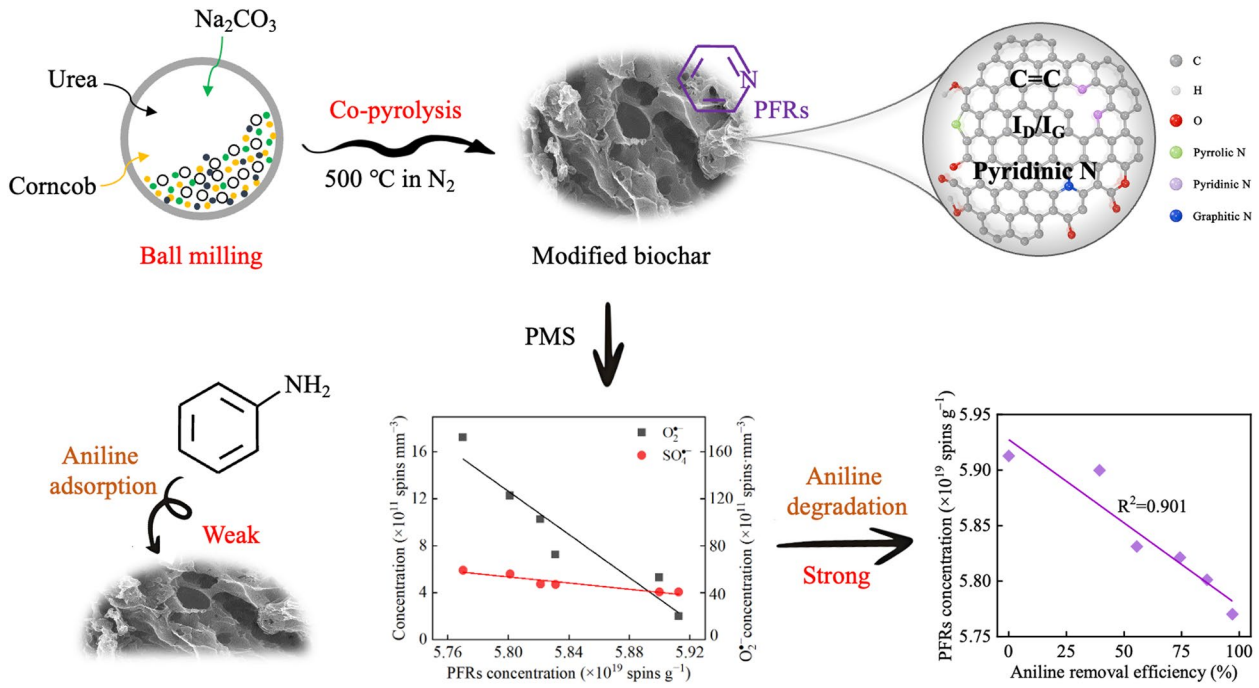

1 Introduction

In recent decades, biochar produced through hydrothermal carbonization or pyrolysis of biomass under anaerobic conditions has gained considerable global attention for its potential in environmental remediation applications (Chen et al. 2024; Wen et al. 2024). Its high specific surface area, well-developed pore structure, and unique chemical properties make biochar an effective catalyst for activating peroxymonosulfate (PMS) to treat recalcitrant organic pollutants in water, including pharmaceuticals, personal care products, endocrine disruptors, volatile organic compounds, and disinfection by-products (Qi et al. 2020; Wu et al. 2021). Research studies indicate that biochar can activate persulfate through multiple active sites, including defective structures, graphitic configurations, oxygenated functional groups, metal species, and persistent free radicals (PFRs) (Luo et al. 2019; Qi et al. 2020; Zhang et al. 2023; Zhao et al. 2021). Among these, PFRs, which could be formed from the partially pyrolyzed organic components of the biomass feedstocks, and/or the stabilized complexation of organic free radicals with transition metals, are one of the most common redox-active sites on biochar. Unlike transient radicals such as ·OH and $SO_4^{\cdot-}$, these solid-phase radicals display higher stability, persisting from hours to years (Ruan et al. 2019). Due to their delocalized unpaired electrons and excellent electron conductivity, PFRs on the biochar surface can transfer single electrons to oxidants, such as HSO_5^-, H_2O_2, and molecular O_2. This process generates reactive oxygen species (ROSs) that can effectively oxidize a range of contaminants, including 2-chlorobiphenyl, diethyl phthalate, 1,3-dichloropropene, sulfamethoxazole, and As(III) (Yuan et al. 2022; Liu et al. 2024a, b; Liu et al. 2020; Luo et al. 2021; Zhu et al. 2023). PFRs can also directly induce the breakdown of organic pollutants like nitrophenol, and mediate the direct reduction of Cr(VI) in aqueous solutions (Hu et al. 2024). It is clear that PFRs play a crucial role in pollutant removal, and in some cases, they even dominate the mechanism (Zhang et al. 2024). However, the importance of PFRs in these processes was often overlooked and has only begun to receive more attention over the past five years (Luo et al. 2021).

Due to the inherent limitations of unmodified biochar in catalytically removing organic pollutants (Zhao et al. 2021), numerous studies have employed various surface modification techniques, including physical/chemical activation and hetero-atom doping (Luo et al. 2021), to enhance the catalytic activity of biochar and broaden its environmental applications. These strategies aim to create specific structures, increase the number of active sites and surface defects, and enhance the specific surface

area, pore size distribution, surface charge, functional groups, and electrical properties of biochar catalysts (Luo et al. 2019; Zhao et al. 2021; Zhu et al. 2018). This significantly enhances PMS activation through radical and non-radical mechanisms, leading to more effective pollutant removal. However, most studies rarely address the impact of these modification methods on PFRs formation and their contribution to the reaction activity of the modified biochar. Understanding these aspects is crucial, as it provides valuable theoretical and practical insights into regulating the properties of biochar, improving its efficiency, and gaining a deeper understanding of the underlying reaction mechanisms.

It is well established that the presence of heterogeneous materials in biomass can significantly affect the behaviour of biomass during thermochemical conversion processes (Huang et al. 2022), leading to variations in the generation and characteristics of PFRs on different biochar surfaces. Since the factors influencing the concentrations and types of PFRs differ across studies, mechanisms by which individual physical/chemical activation or hetero-atom doping influences PFR formation on biochar surfaces remain controversial. For example, HNO_3 activation alters the surface characteristics of pyrolyzed biochar and increases the number of biochar-PFRs, particularly the oxygen-centered radicals (Luo et al. 2019). However, it does not substantially increase the concentration of PFRs in hydrochar (Yan et al. 2018). Moreover, heteroatom doping is believed to alter the distribution and content of C and O atoms within the biochar structure, thereby influencing the concentration and type of PFRs (Yu et al. 2020). Some researchers suggest that heterocycles in biomass could regulate unpaired electrons on adjacent sp^2-hybridized carbon substrates, facilitating PFRs formation within biochar (Yu et al. 2020). However, other studies suggest that nitrogen from urea can replace oxygen in –OH groups within biochar to form $–NH_2$, which may consume PFRs. This is supported by observations of negative correlation between PFR intensity and nitrogen content (Bi et al. 2022; Huang et al. 2022; Wu et al. 2021). With the combined modifications, a synergistic activation effect is often observed. For example, the combined activation of an alkali chemical like KOH and N-dopants such as urea, can promote the formation of additional microporous structures and enhance the selectivity of catalytic reactions (Lin et al. 2023). These interactions undoubtly add complexity to studying PFRs. Given the intricate, non-linear relationship between biomass carbonization conditions and PFR characteristics, it is essential to understand how PFR occurrence relates to elemental composition, microstructure, and surface properties during carbonization. Establishing these connections enhances the current understanding of biochar-PFR formation and reaction characteristics under various modification conditions (Chen et al. 2024). To our knowledge, any similar study has not been reported as yet.

In this study, corncob, sodium carbonate (Na_2CO_3) as an alkali chemical, and various nitrogen precursors were ball-milled and co-pyrolyzed to synthesize modified biochars. The effects of pyrolysis temperature and modification methods on PFR formation in biochar were systematically investigated. The Spearman analysis was used to assess correlations between elemental composition, structural characteristics, functional group composition, and PFR formation during co-pyrolysis, clarifying the key factors influencing PFR formation under combined modification with heteroatoms and Na_2CO_3, as well as possible synergistic effects. The catalytic and adsorption performance of the modified biochar was then evaluated, using aniline as the target contaminant due to its widespread industrial use and substantial threat to ecosystems and human health upon enetring water. The potential mechanism by which biochar-PFRs activate PMS for aniline degradation was further examined by indentifying reactive species and analyzing their correlation analysis with aniline removal. The findings from this study provide fundamental insights into PFR generation on biochar surfaces during biomass co-pyrolysis with different modifiers and highlight the predominant roles of these PFRs in the removal of recalcitrant organic pollutants, supporting the development of biochar tailored for specific environmental applications.

2 Materials and methods

2.1 Materials

The corncob used as the precursor for biochar production was obtained from Jiangsu Surui Straw Processing Factory. Before use, it was washed, dried, and ground into a fine powder with a 100–200 mesh particle. Elemental analysis revealed that the corncob contained 47.21% carbon, 6.25% hydrogen, 45.70% oxygen, 0.74% nitrogen, and 0.10% sulfur. When combusted at 550 °C, the corncob ash was primarily composed of SiO_2 (76.20%), K_2O (8.37%), and CaO (4.18%), with additional components provided in the Supplementary Materials Table S1. All chemical reagents used in this study were of guaranteed reagent or analytical reagent grade. Aniline ($C_6H_5NH_2, \geq 99.5\%$), peroxymonosulfate (PMS, $2KHSO_5{\cdot}KHSO_4{\cdot}K_2SO_4$, 42%), sodium carbonate ($Na_2CO_3, \geq 99.5\%$), dicyandiamide ($C_2H_4N_4$, 99%), melamine ($C_3H_6N_6$, 99%), thiourea (CH_4N_2S, 99%), urea (CH_4N_2O, 99%), methanol (MeOH, 99%), *tert*-butanol (TBA, 99%), *p*-benzoquinone (*p*-BQ, 99%), furfuryl alcohol (FFA, 99%), potassium iodide (KI, 99%), hydrochloric acid (HCl, 37%), sodium hydroxide (NaOH, 96%), and sodium thiosulfate ($Na_2S_2O_3$, 98.0%)

were obtained from Aladdin Reagent (Shanghai) Co. 5,5-dimethyl-1-pyrroline N-oxide (DMPO, 97%), and 2,2,6,6-Tetramethylpiperidine (TEMP, > 98.0%) were procured from Sigma-Aldrich Chemical Company. Deionized water with a resistance of 18 MΩ cm was consistently used throughout the experiments.

2.2 Modified biochar preparation

Modified biochar was synthesized through a co-pyrolysis process. Based on preliminary experiments (Fig. S1), 3.0 g of corncob was ball-milled with 4.0 g of an N precursor (urea, dicyandiamide, melamine, or thiourea) and 3.0 g of Na_2CO_3 for 1 h to form a uniform mixture. The mass percentages of these components were 30%, 40%, and 30%, respectively. This mixture was then pyrolyzed in a tube furnace at set temperatures (300 ℃, 400 ℃, 500 ℃, 600 ℃, 700 ℃, and 900 ℃) for 2 h under N_2 atmosphere, with a heating rate of 10 ℃ min^{-1}. After cooling to room temperature, the solid residues were rinsed several times with deionized water and ethanol, then oven-dried at 70 ℃, ground, sieved through a 100-mesh sieve, and vacuum-sealed for storage. The resulting samples were labelled MBX, where X represents the pyrolysis temperature. For comparison, unmodified biochar samples (CK) and samples modified with different mass ratios of Na_2CO_3 to N precursor were prepared under similar conditions.

2.3 Batch experiments

Pollutant degradation experiments were conducted at 25 °C in a 100 mL beaker containing 50 mL of aqueous aniline solution (10 mg L^{-1}, pH approximately 7). The initial pH was adjusted using either 0.1 M HCl or 0.1 M NaOH. Typically, a predetermined amount of catalyst (0.035 g) was added to the aniline solution under magnetic stirring, and PMS (0.01 g) was then introduced to initiate the reaction. At specific time intervals, 1 mL of the reaction mixture was filtered through a 0.22 μm filter and mixed with a measured volume of $Na_2S_2O_3$ for analysis. After the reaction, the catalyst was recovered by filtration, washed several times with deionized water, dried at 70 ℃ for 12 h, and subjected to recycling tests. Single-factor experiments were performed to evaluate the effects of initial solution pH (3–10), pollutant concentration (5–25 mg L^{-1}), PMS concentration (0.025–0.05 g L^{-1}), and catalyst dosage (0.2–0.9 g L^{-1}) on aniline removal efficiency. Aniline degradation in the optimized catalytic system with different concentrations (5–200 mg L^{-1}) of Cl^-, NO_3^-, $HCO_3^-$and CO_3^{2-} was also investigated. Parallel tests were conducted with various scavengers, including MeOH, TBA, *p*-BQ, FFA, and KI to identify the reactive species involved in aniline degradation. Furthermore, adsorption experiments were carried out under identical conditions, but without adding PMS. At specific time intervals, 1 mL of the sample was collected, filtered through a 0.22 μm filter, and prepared for analysis. All experiments were performed in triplicate, with error bars in the figures representing the standard deviation from these three independent trials.

2.4 Characterization and analysis methods

The elemental contents of C, H, O, N, and S in the samples were determined using Unicube elemental analyzer (Elementar). The inorganic components of corncob biomass were analyzed using an X-ray fluorescence spectrometer (XRF, ZSX Primus III+, Rigaku). Fourier transform infrared (FTIR) spectrum was recorded using the KBr pellet method on an FTIR spectrometer (Scientific Nicolet iN10, Thermo Fisher) with a scanning range from 400 cm^{-1} to 4000 cm^{-1}. The contents of oxygenated functional groups, including phenolic hydroxyl, lactone, and carboxyl, were assessed using the Boehm titration method. The surface elemental composition and chemical states were analyzed via X-ray photoelectron spectroscopy (XPS, Scientific ESCALAB Xi+, Thermo Fisher) with Al Kα (12.5 kV) as the X-ray source, using C1s at a binding energy of 284.8 eV as an internal standard. Raman spectra were recorded using a confocal Raman microscope (alpha300R, WITec) equipped with 532 nm laser, covering a spectral range of 40–4000 cm^{-1}. The surface Zeta potential of the sample was measured using a nanoparticle size and Zeta potential analyzer (DLS, Zetasizer Nano ZS90, Malvern).

Aniline concentration was measured using high performance liquid chromatography (HPLC, Acquity H-Class, Waters) equipped with a reversed-phase C18 column (5 μm × 4.6 mm × 250 mm) and a UV detector set at 230 nm. The mobile phase (10 mL) for aniline consisted of a 45:55 (v/v) acetonitrile and deionized water mixture, with a flow rate of 0.25 mL min^{-1}. The concentrations and types of PFRs in the biochar were analyzed using an electron paramagnetic resonance spectrometer (ESR, Magnettech ESR5000, Bruker). The generation of possible reactive species, such as ·OH, $SO_4^{\cdot-}$, $O_2{\cdot}^-$, and $^1O_2$, was investigated with an EPR spectrometer (EMXplus-6/1, Bruker), employing DMPO and TEMP as trapping agents. Further details on the Boehm titration and EPR procedures are provided in Text S1.

3 Results and discussion

3.1 Impact evaluation of PFRs formation during pyrolysis

The formation and evolution of PFRs during pyrolysis are significantly influenced by the pyrolysis temperature (Chen et al. 2024; Zhang et al. 2023). As illustrated in Fig. 1, the concentration of PFRs progressively increased with rising pyrolysis temperatures, reaching

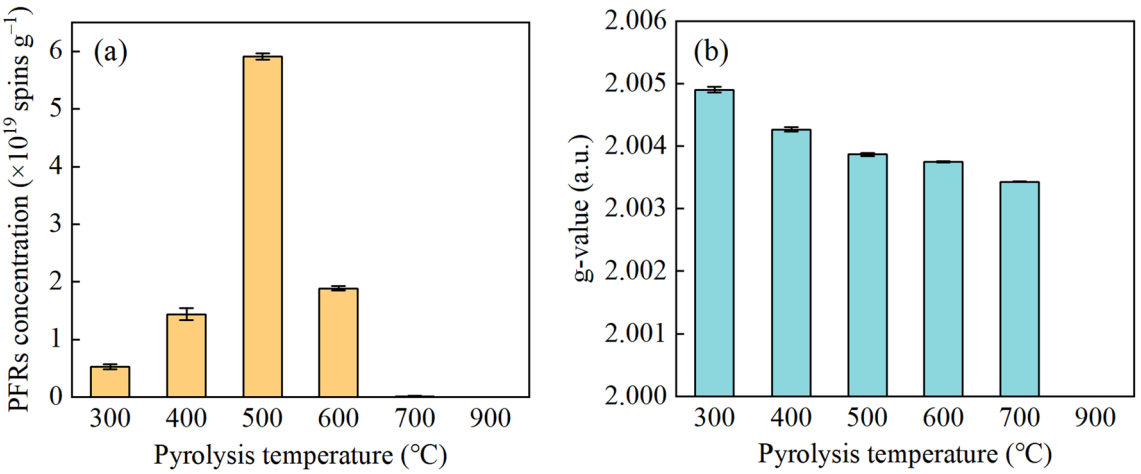

Fig. 1 Effect of pyrolysis temperature on PFRs concentrations (**a**) and their g-values (**b**)

a maximum of 5.91×10^{19} spins g^{-1} at 500 ℃. This peak concentration is consistent with previously reported values, which typically range from 10^{16} to 10^{19} spins g^{-1} (Luo et al. 2021). Beyond this temperature, the concentration of PFRs dropped sharply or even vanished, likely due to the breakdown and reorganization of the organic structure, as well as a decrease in the availability of phenolic compound precursors (Luo et al. 2021; Yang et al. 2016; Zhang et al. 2023). This pattern differs from the typical changes observed in the pore structure of biochar during pyrolysis (see Fig. S2). With increasing pyrolysis temperature, biochar undergoes thermoplastic transformations, forming macropores and micropores. This process resulted in a steady rise in specific surface area and pore volume, reaching 1224.58 m^2 g^{-1} and 0.99 cm^3 g^{-1}, respectively. In contrast, the average pore size consistently exhibited mesoporous characteristics (ranging from 3.22 to 41.52 nm) and gradually decreased (see Table S2). Regarding the g-value, pyrolysis temperatures between 300 and 400 ℃, yielded values above 2.0040, indicating a predominance of oxygen-centered semiquinone-type PFRs. However, at temperatures between 500 ℃ and 700 ℃, the g-value fell within the range of 2.0030 to 2.0040, suggesting a co-prevalence of both carbon and oxygen-centered phenoxy PFRs (Bi et al. 2022). Previous studies indicate that with increasing temperature and pyrolysis duration, the types of PFRs on the biochar surface transition from semiquinone-type radicals to phenoxy-type radicals and eventually to cyclopentadienyl radicals (Huang et al. 2022; Luo et al. 2021; Ruan et al. 2019). This transformation coincides with the gradual reduction of oxygenated functional groups, including phenols, alcohols, lactones, aldehydes, ketones, and carboxylic acids, as confirmed by FTIR analyses and Boehm titration results (Fig. S3). Given that the highest concentration of PFRs was observed at 500 ℃, the MB500 sample was chosen as the representative sample for subsequent analysis.

Further investigation examined the impact of biochar modification methods on PFRs formation. As shown in Fig. 2a, after pyrolysis at 500 ℃, the concentration of PFRs on unmodified corncob biochar was 4.08×10^{19} spins g^{-1}, primarily consisting of carbon- and oxygen-centered free radicals. Biochar modification notably affected the concentration of PFRs, while having little impact on the types of radicals present (Fig. 2b). Under modification conditions, the g-value typically showed a slight increase, indicating a higher proportion of oxygen-centered PFRs. Previous studies have reported that oxygen-centered PFRs are more reactive than carbon-centered PFRs, particularly in generating reactive species such as $SO_4^{\cdot -}$ radicals (Yu et al. 2020). Unlike the adverse effects induced by Na_2CO_3 activation, urea addition alone tended to facilitate the production of more PFRs. Interestingly, the combined use of Na_2CO_3 and urea resulted in a significant synergistic enhancement of PFRs concentration. As the mass ratio of urea to Na_2CO_3 increased from 1:4 to 2:1, the PFRs concentration first rose and then decreased, peaking at a mass ratio of 3:4. According to literature, Na_2CO_3 lowers the activation energy during pyrolysis, promoting the condensation of small organic molecules into conjugated aromatic rings. This process also generates numerous defective edges along the biochar boundaries, introducing hydrogen and oxygen functionalities (Huang et al. 2022; Qi et al. 2020; Tao et al. 2020). A high proportion of Na_2CO_3 in the mixture may lead to sodium ions occupying active sites on the benzene ring, thereby reducing the potential for alkyl or aliphatic side chains to participate in cyclization reactions.

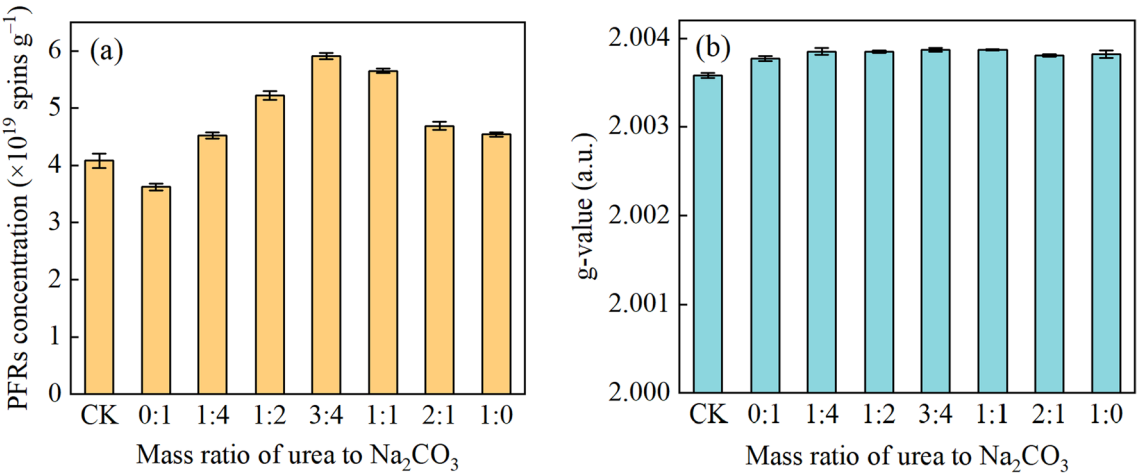

Fig. 2 Effect of modification methods on PFRs concentrations (**a**) and their g-values (**b**)

This interference inhibits the condensation of polycyclic aromatic hydrocarbons (PAHs), which in turn limits the availability of precursor compounds essential for the formation of PFRs. Consequently, an excess of Na_2CO_3 may reduce the overall concentration of PFRs by disrupting the molecular processes that facilitate their generation (Huang et al. 2022). The inclusion of urea tends to disrupt carbon layers, forming heterocycles and generating more defects in MB500 (Wu et al. 2021; Zhu et al. 2018). These defects could regulate unpaired electrons onto the adjacent carbon structures, generating more lone pair electrons within PFRs (Liu et al. 2024a, b). Excessive nitrogen doping can release substantial amounts of nitrogen-containing small molecules, such as NH_3, which may react with hydrocarbon radicals (e.g., ·CH). This reaction can quench certain PFRs, leading to a reduction in their overall concentration. Consequently, maintaining an optimal ratio of urea to Na_2CO_3 is essential to enhance the synergistic effects between these components, thereby promoting PFR generation. Furthermore, the molecular structure of nitrogen precursors plays a significant role in influencing the condensation behavior of biochar and surface property changes during pyrolysis, affecting both the concentration and types of PFRs formed (Fig. S4a and Fig. S4b). For instance, the PFR concentration in MB500 increased when using urea, dicyandiamide, or melamine as nitrogen precursors. A related study noted that, despite dicyandiamide and melamine having higher nitrogen content than urea, they tend to form more condensed C_XN_y structures (such as CN heterocycles and tri-s-triazine units) during pyrolysis, where nitrogen is not fully incorporated into the carbon lattice. In contrast, the thermal decomposition of urea produces NH_3 and CO_2, which facilitates N-doping, tailors the surface chemistry and pore structure of the biochar, and modifies the acidity and alkalinity of the graphene basal plane (Li et al. 2017). As a result, urea achieved a high level of N-doping in the biochar, establishing a more favorable microenvironment for PFR generation (see Sect. 3.2). In contrast, using thiourea inhibited PFR formation in MB500. The expected synergistic effect of N,S co-doping did not occur; instead, N,S co-doping appears to substitute more oxygen atoms, resulting in fewer defect structures in the biochar compared to the single N-doped system (Ding et al. 2020; Zhang et al. 2022a, b). In summary, compared to dicyandiamide, melamine, and thiourea, urea-modified biochar produced the highest concentration of PFRs on its surface under the same dosage conditions. Meanwhile, based on the results of the preliminary experiments, it was also found that a higher concentration of PFRs correlates with a higher removal efficiency of aniline (Fig. S4c). Thus, urea can be chosen as the N precursor for biochar modification in future experiments to further explore PFR generation and its relationship with pollutant removal.

3.2 Correlation between influence factors and PFRs formation

During biomass pyrolysis, the formation of PFRs with unpaired electrons is driven by chemical bond cleavage and carbon structure reconstruction, involving a series of reactions (Chen et al. 2024; Tao et al. 2020) which may include dehydration, decarboxylation, decarbonylation, aromatization, and intra-molecular condensation (Huang et al. 2022; Ruan et al. 2019; Tao et al. 2020; Wu et al. 2021). Due to the complexity and interdependence of these fundamental reactions, the modified biochars produced at pyrolysis temperatures from 300 to 600 ℃ were quantitatively characterized for their elemental composition, structural features, and types of functional

groups. Since biochar modification affects PFR concentration more than PFR type, Spearman analysis was conducted to explore correlations between these quantitative indicators and PFR levels. This analysis aimed to deepen the understanding of PFR formation in biochar modified with both urea and Na_2CO_3.

As shown in Fig. 3 and Fig. S5, there was no significant positive or negative correlation between PFRs concentration and most quantitative indicators except for C=C ($P \leq 0.05$), I_D/I_G ($P \leq 0.01$), and pyridinic N ($P \leq 0.01$). As pyrolysis temperature rises, covalent bonds between substituent groups (such as methylene and methyl) and functional groups (like C–C and C–O–C bonds) in biomass progressively break, generating numerous free radical fragments that recombine to form aromatic rings. These rings then condense to form larger, fused aromatic structures, stabilizing PFRs due to steric hindrance (Chen et al. 2024; Ruan et al. 2019). Similar findings have been reported, suggesting that phenolic O–H groups may convert to phenoxy, with aromatization leading to the formation of aromatic radicals, as indicated by an increase in C=C bonds in aromatic and heterocyclic rings (Zhu et al. 2023). This implies that PFR formation is highly dependent on aromatic C=C structures. The structural indicator I_D/I_G shows a significant positive correlation with PFR concentration ($P \leq 0.01$), underscoring the role of defect structures in PFR generation. These abundant structural defects generally enhance the transport of unpaired electrons, resulting in increased free radical production. (Zhu et al 2018). The significant correlation between the relative content of pyridinic N and PFRs concentration further indicates that among various defect structures, pyridinic N significantly plays a particularly crucial role in PFRs generation. Due to the specific electron configuration, pyridinic N with sp^2 hybridization at the edges of graphene planes could raise the density of p states near the Fermi level and lower the work function, thus serving as active sites (Yu et al. 2020) promoting PFRs formation by providing provide *p*-electrons to the π system (Wu et al. 2021). XPS analysis (Fig. S6) showed that addition of Na_2CO_3 alone increased the pyrrolic N content in biochar from 34.6 to 59.69%, while urea alone promoted an increase in both pyridinic N and graphitic N, particularly in graphitic N, which rose from 10.96 to 24.2%. However, combining urea and Na_2CO_3 significantly enhanced the pyridinic and pyrrolic N content in biochar while reducing graphitic N and oxidized N levels. This suggests that the combined modification with urea and

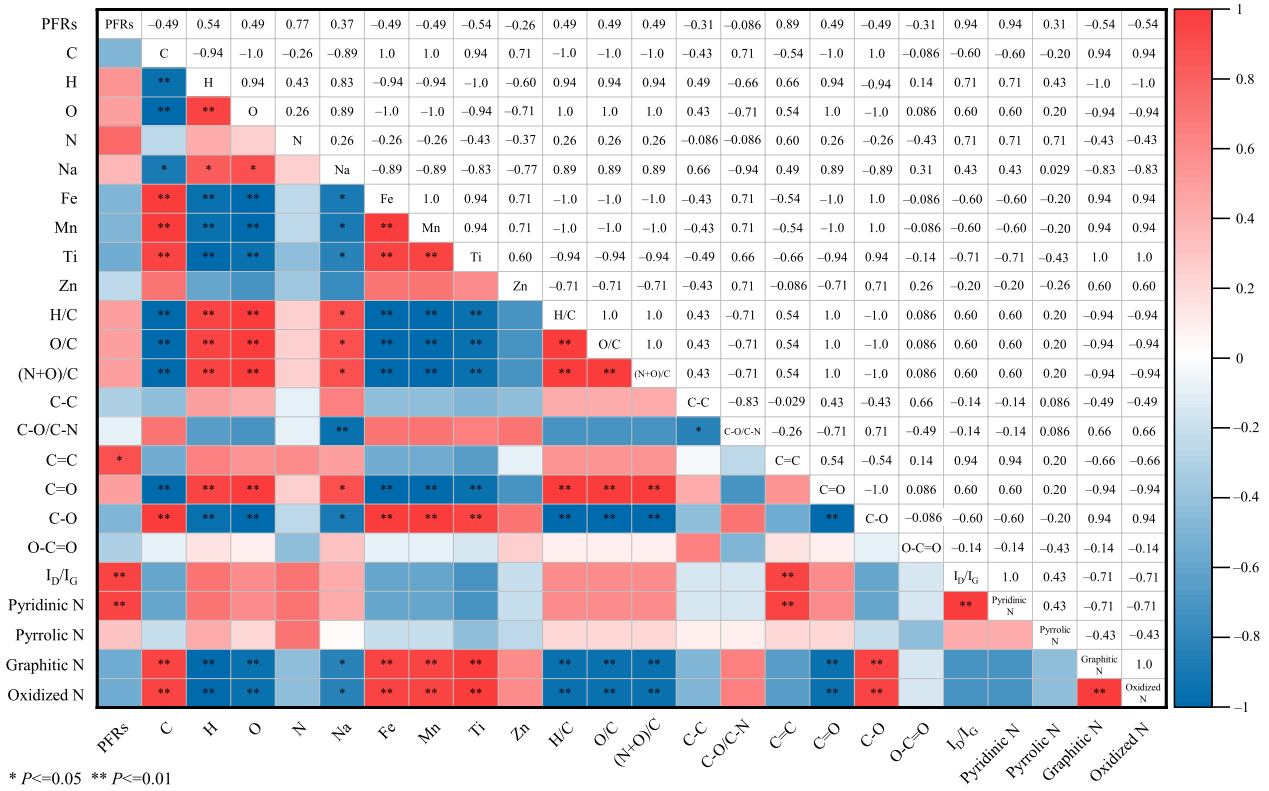

* P<=0.05 ** P<=0.01

Fig. 3 Spearman correlation analysis between PFRs concentration and various characteristic indicators of biochar

Na_2CO_3 may help slow the conversion of pyridinic and pyrrolic N into graphitic N during pyrolysis (Zhao et al. 2021), favoring the creation of nitrogen heterocyclic structures in biochar.

Although no significant correlation was found between other factors and PFRs formation, they still have a combined effect on the generation and stabilization of PFRs. Biochar produced at moderate temperatures primarily forms oxygen-centered or carbon- and oxygen-dentered PFRs, indicating that the presence of oxygen or other elements is essential for enhancing PFRs generation, even though carbon is the primary element involved in PFRs formation (Bi et al. 2022). For example, due to their small size and high reactivity, H radicals can easily enter the macromolecular carbon skeleton structure and participate in the pyrolysis reaction. A higher number of H radicals may lead to a reduction in carbon-centered PFRs in biochar (Chen et al. 2024), while a higher presence of oxygen-containing structures, particularly quinones, can promote the formation of more PFRs (Wu et al. 2021). The positive correlation between PFRs concentration and the content of residual N and Na in biochar suggests that the synergistic effect of urea and Na_2CO_3 promotes the formation of PFRs. This aligns with the observed correlations between PFRs concentration and the relative content of pyridinic N. Similar influence was also reflected in other structural indicators, including the H/C, O/C, and (O + N)/C atomic ratios, which represent the degree of aromatization, the quantity of oxygenated functional groups, and the polarity of biochar, respectively.

In terms of inorganic elements, it is generally accepted that trace concentrations of transition metals act as electron acceptors, extracting delocalized π-electrons from substituted aromatics in biochars (e.g., hydroquinone or catechol) and controlling the types and intensities of PFRs (Liu et al. 2024a, b; Ruan et al. 2019). However, excessive metal contents in biomass may consume the unpaired electrons for nucleation and reduction of metals (Wu et al. 2021; Liu et al. 2024a, b) due to the electron-shuttling effect of PFRs (Ruan et al. 2019). Unlike Fe, Zn in corncob biomass may suppress PFRs formation by hindering the electron transfer during biomass pyrolysis due to its poor ability to accept electrons (Liu et al. 2024a, b). This complex relationship negatively impacts PFRs formation.

The intensity of PFRs shows a positive correlation with C=O and pyrrolic N, and a negative correlation with C–O, O–C=O, graphitic N, and oxidized N. It has been suggested that KBH_4-reducible carbonyl groups, likely present in aldehydes, aromatic ketones, and quinone structures (Liu et al. 2024a, b), are important indicators of PFRs in biochars. These structures are associated with PFR formation, particularly in the reversible reaction between semiquinone radicals and quinones (Liu et al. 2024a, b; Tao et al. 2022). The homolytic cleavage of C–O or O–C=O linkages is a prerequisite for PFRs formation during biomass pyrolysis (Chen et al. 2024), so their contents are negatively correlated with PFR concentration. For pyrrolic N, it has been stated that PFRs formed within the pyrrolic N structure are more delocalized and stable compared to those in the graphitic-N structure. This is due to the lower energies of singly occupied molecular orbitals (SOMOs) and the distinct charge distribution patterns in the pyrrolic N structure (Zhu et al. 2020). Therefore, the presence of pyrrolic N is more conducive to PFRs formation. Based on the above discussion, it can be concluded that C=C ($P \leq 0.05$), I_D/I_G ($P \leq 0.01$), and pyridinic N ($P \leq 0.01$) are the key factors in regulating PFRs formation in MB500 catalysts. The pyridinic ring, whether or not it contains oxygenated functional groups, is likely the primary source of PFRs. However, due to the limited scope of research conducted, the complex relationships between the elemental composition, structural characteristics, functional group types, and PFR properties of biochar remain inadequately understood. A more detailed investigation is needed in future studies to fully elucidate these connections.

3.3 Catalytic performance and reusability of MB500 for aniline removal

Aniline, a widely used organic compound in various industrial applications, was selected as a target pollutant to evaluate the catalytic performance of the MB500 catalyst towards PMS in aqueous solutions under different conditions. Figure 4a and b illustrate the influence of initial pH on aniline removal. At pH 3, the MB500/PMS catalytic system demonstrated relatively low aniline removal, likely due to the stabilizing effect of excess H^+ ions (Zhao et al. 2021). However, as the initial pH increased from 4 to 9, aniline removal progressively improved, indicating that neutral and alkaline conditions are conducive to generating more reactive species. At an initial solution pH of 7–9, a PMS concentration of 0.2 g L^{-1} and an MB500 dosage of 0.7 g L^{-1}, the MB500/PMS catalytic system achieved maximum aniline removal (90–92%) at 10 mg L^{-1} within 30 min, at a rate constant of 0.074–0.083 min^{-1}. Raising the initial pH to 10 resulted in a dramatic decrease in aniline removal efficiency, indicating a significant drop in performance. This inhibition was likely due to the self-decomposition of PMS, resulting in inefficient oxidant consumption (Zhao et al. 2021). When the aniline concentration was increased to 25 mg L^{-1}, the removal efficiency and rate constant dropped to 87.68% and 0.068 min^{-1}, respectively (Fig. 4c and d). The decrease is likely due to insufficient PMS or catalyst in the system.

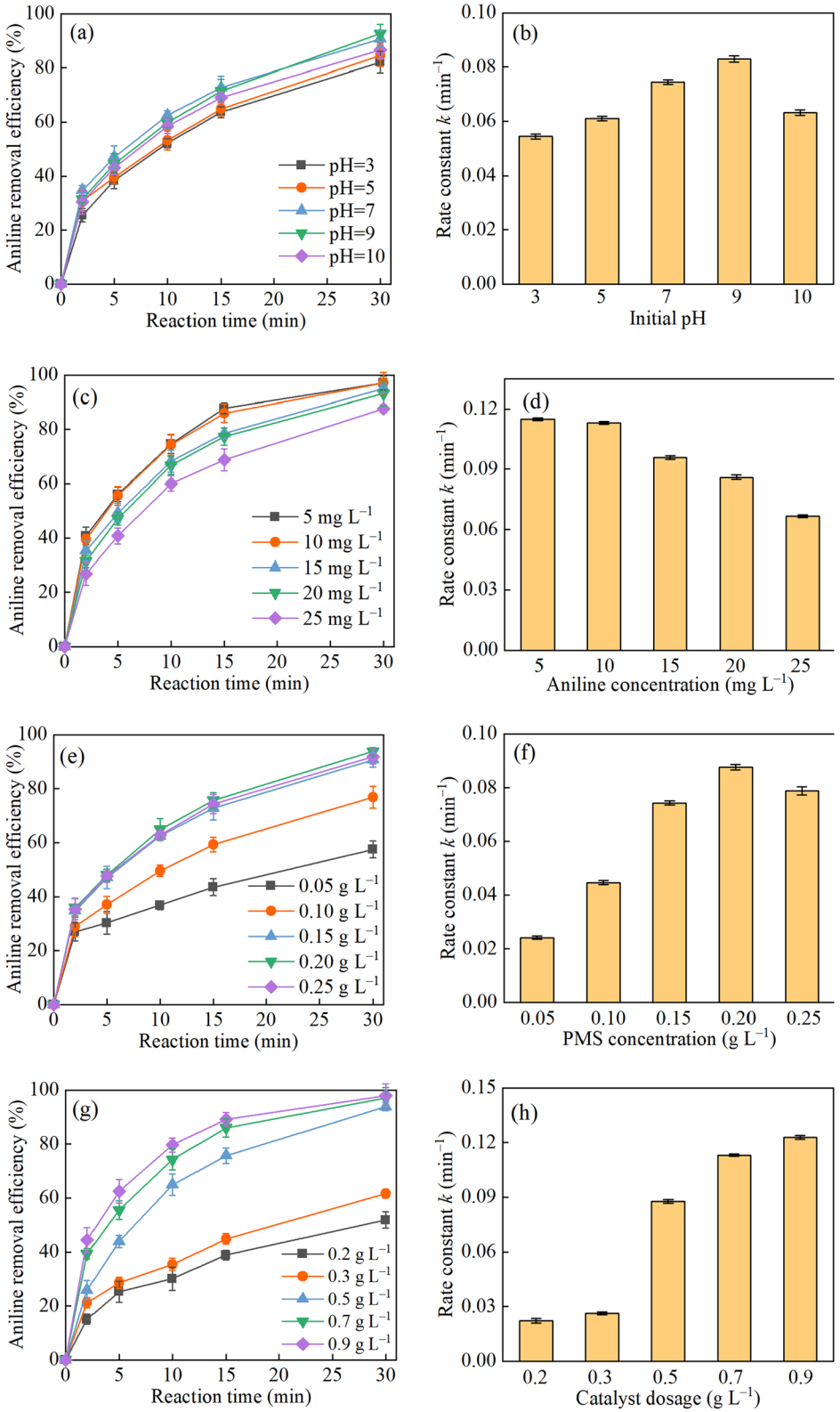

Fig. 4 Effect of initial pH (**a**, **b**) (aniline concentration = 10 mg L^{-1}, PMS concentration = 0.15 g L^{-1}, MB500 dosage = 0.5 g L^{-1}), aniline concentration (**c**, **d**) (initial pH = 7, PMS concentration = 0.2 g L^{-1}, MB500 dosage = 0.7 g L^{-1}), PMS concentration (**e**, **f**) (initial pH = 7, aniline concentration = 10 mg L^{-1}, MB500 dosage = 0.5 g L^{-1}), and catalyst dosage (**g**, **h**) (initial pH = 7, aniline concentration = 10 mg L^{-1}, PMS concentration = 0.2 g L^{-1}) on aniline removal efficiency and reaction rate constant in the MB500/PMS catalytic system

Adding more PMS or catalyst can introduce additional active sites and reactive species, thereby improving the aniline removal process (Fig. 4e–h). The MB500/PMS catalytic system maintained stability against Cl^- and NO_3^-, even at elevated concentrations. (200 mg L^{-1}; Fig. S7). This stability may originate from the generation of additional reactive species like Cl·, Cl_2, HOCl, $^1O_2$, and NO_3· throughout the reaction process, which help maintain catalytic activity (Zhao et al. 2021). However, the presence of HCO_3^- and CO_3^{2-} has a significant inhibitory effect at a concentration of 200 mg L^{-1} on aniline removal, particularly CO_3^{2-}. This inhibition primarily arises from the ability of CO_3^{2-} and HCO_3^- to capture ·OH, $SO_4^{\cdot-}$, and $O_2\cdot^-$, forming less reactive species like $CO_3\cdot^-$ and $HO_2\cdot^-$. Moreover, the presence of CO_3^{2-} and HCO_3^- anions may lead to an increase in solution pH, which is unfavourable for aniline removal (Liu et al. 2023). Despite these problems, aniline removal performance remained high (90.88% for HCO_3^- and 81.43% for CO_3^{2-}), implying an outstanding tolerance of the MB500/PMS catalytic system to anions.

The reusability of the modified biochar catalyst is a critical metric for assessing its long-term effectiveness. As illustrated in Fig. S8, after five consecutive reuse cycles, the aniline removal efficiency of the MB500/PMS catalytic system gradually decreased from an initial 97.02% to 78.91%. This decline can be attributed to several factors, as EPR and XPS analyses demonstrated. First, the continuous consumption of PFRs during the reaction process led to a reduction in catalytic activity (Fig. 5a). The positive correlation between aniline removal and PFR signals on biochar particles after multiple reuse cycles (Fig. 5b) indicates that the reduction in PFRs significantly contributes to the decline in aniline removal efficiency. Since PFRs primarily originate from the pyridine rings in biochar, the relative content of C=C, C–O/C–N functional groups, and pyridinic N decreased after catalytic reactions (Fig. 6a and b). Secondly, the deposition of oxidation-resistant intermediates on the biochar surface presumably interferes with the catalytic process by blocking active sites and hindering their interaction with PMS and aniline (Luo et al. 2019; Ruan et al. 2019; Zhu et al. 2018). The XPS analysis further these findings, showing an increase in surface carbon content from 73.26 to 76.69% after the catalytic reaction, specifically in C–C bonds (Fig. 6a), Concurrently, the proportions of other key elements, such as nitrogen (decreasing from 13.64 to 12.87%) and oxygen (from 13.11 to 10.43%), reduced. The reduction in other active sites on the biochar surface further impacts its catalytic efficiency. Oxygen containing functional groups such as C=O (ketone carbonyl) and O–C=O (ester or carboxyl groups), along with nitrogen species like graphitic N, underwent varying degrees of consumption during the reaction (Fig. 6a–c), which in turn influenced the generation of reactive species in the system. Importantly, O–C=O bonds herein mainly originate from lactone groups in biochar rather than carboxyl groups (Fig. 6d). Previous studies have suggested that the lone pair of electrons in the Lewis basic sites of biochar-based catalysts (such as the oxygen atom in C=O and pyridinic N), as well as the free-flowing π-electrons in sp2-hybridized carbon, can transfer from the biochar to PMS, thereby inducing the production of ·OH and $SO_4^{\cdot-}$ (Zhang et al. 2023; Zhao et al. 2021). The graphitic N structure enhances the formation of dangling σ bonds and facilitates electron transfer by increasing the charge density of carbon atoms. This, in turn, promotes PMS

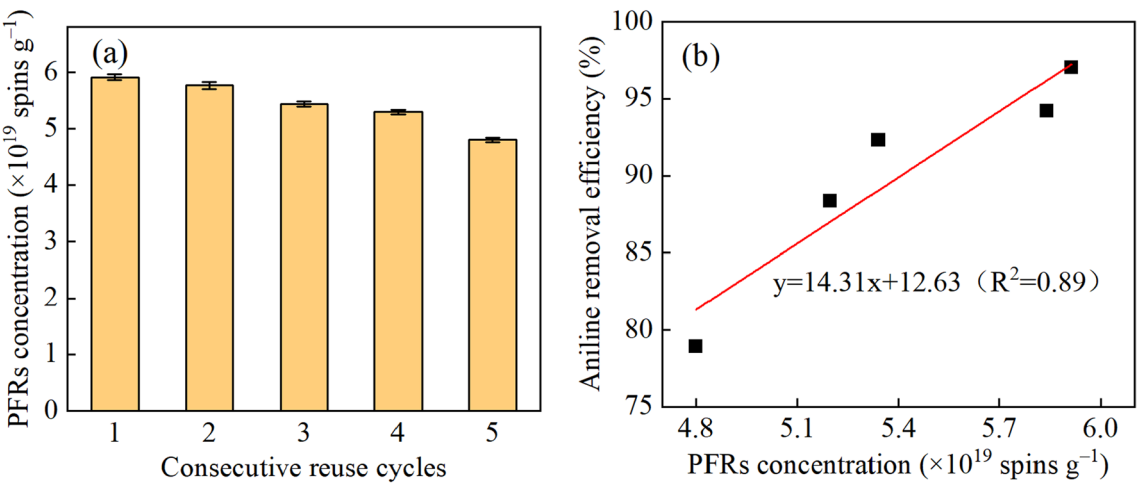

Fig. 5 Effect of repeated cycles on the PFRs concentration (**a**), and correlation between PFRs concentration and aniline removal efficiency in cyclic experiments (**b**)

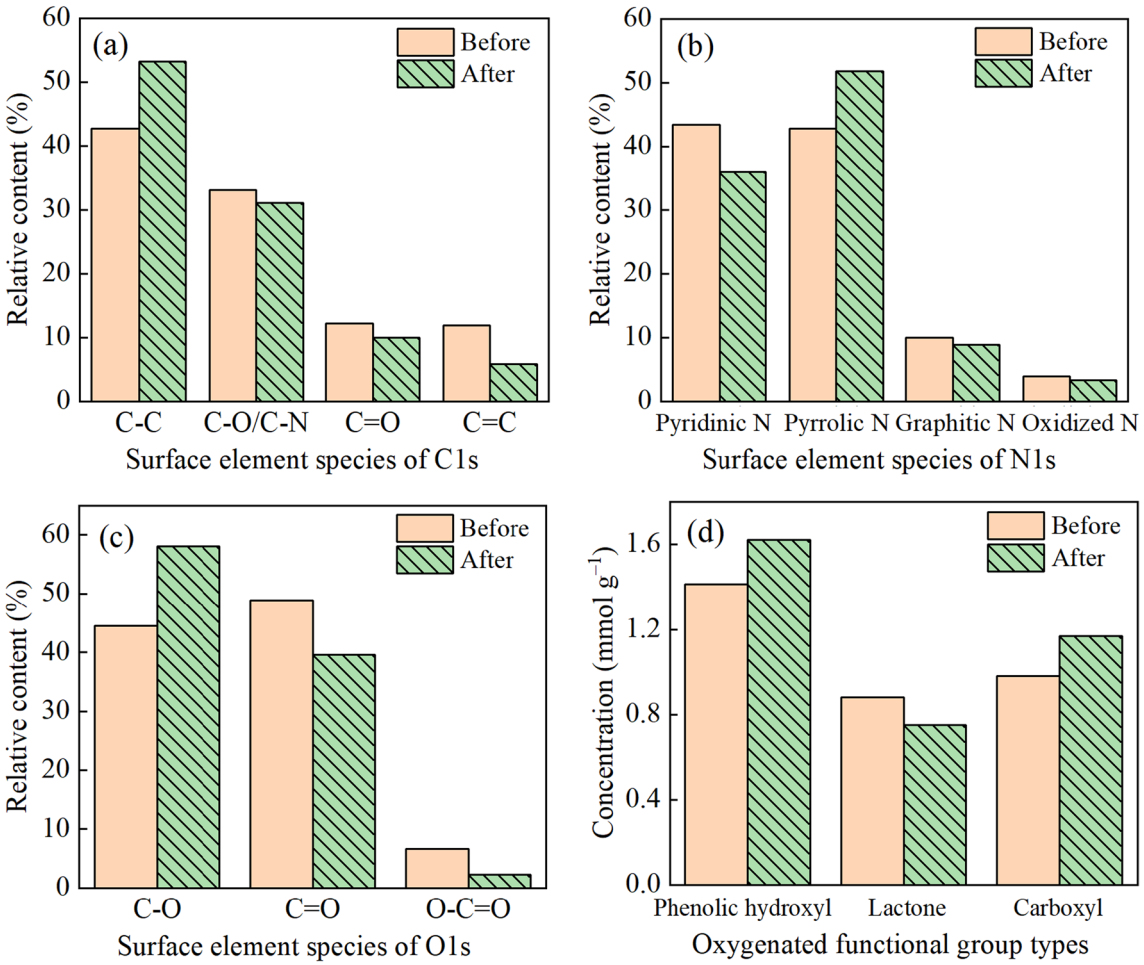

Fig. 6 Changes in relative contents of various C1s (**a**), N1s (**b**), and O1s (**c**) species and the concentrations of oxygen containing functional groups (**d**) on MB500 surface before and after catalytic

adsorption and activation activity via the transfer of electron from biochar to PMS (Luo et al. 2021; Qi et al. 2020; Zhao et al. 2021). As these active sites were consumed, additional C–O functional groups and pyrrolic N were formed on the biochar surface (Fig. 6a–c). These changes in the physicochemical properties of the biochar surface can negatively impact its catalytic performance. It is often overlooked that interactions between biochar and pollutants—driven by factors such as metal cations, reactive oxygen species (ROS), and ultraviolet radiation—may facilitate the regeneration of biochar-PFRs during the reaction (Xie et al. 2024). Therefore, future studies should focus on improving the regeneration of biochar-PFRs.

3.4 Adsorption behavior of MB500 catalyst

In the biochar/PMS catalytic system, the removal of organic pollutants generally involves both adsorption and degradation mechanisms (Luo et al. 2021). Fig. S9 illustrates the adsorption hebavior of MB500 towards aniline at different initial pH levels. The results indicated that within the initial pH range of 3 to 10, aniline adsorption tended to equilibrium in approximately 30 min, with removal efficiencies ranging from 19.89 to 30.27%. As the initial pH increased, the removal efficiency decreased, suggesting that the moderate adsorption capacity of MB500 did not play a significant role in aniline removal in the MB500/PMS catalytic system. The adsorption of aniline on MB500 followed pseudo-second-order kinetics, with a high correlation coefficient of $R^2 = 0.996$ (Fig. S10 and Table S3), indicating the predominance of chemical adsorption. In this case, the physical adsorption facilitated by the porous structure, characterized by a specific surface area of 48.74 $m^2\ g^{-1}$, a pore volume of 0.10 $cm^3\ g^{-1}$, and an average pore size of 8.46 nm contributed minimally to the overall activity of the optimal catalyst. Interestingly, in an extended adsorption study, the removal rate of aniline increased steadily over time, ultimately reaching 40% after 40 days (Fig. 7). Given

the reaction characteristics of PFRs, it is reasonable to hypothesize that PFRs in biochar can directly react with aniline, leading to its oxidative degradation. Previous studies have also reported that PFRs, with their delocalized unpaired electrons, can remediate pollutants by regulating electron transfer independently (Liu et al. 2024a, b; Yang et al. 2016). Due to the slow nature of the direct degradation process, no systematic or in-depth research was conducted on it in this study.

The pH of a solution significantly influences the types of pollutants, the surface charge of biochar, and other physicochemical properties, thereby interfering with the adsorption behaviour of biochar. According to the Zeta potential distribution graph (Fig. S11), the isoelectric point of MB500 was 1.90. Within the pH range of 3 to 10, the surface of MB500 consistently carried a net negative charge, with the degree of deprotonation increasing as the pH rose. Aniline, a weak base, predominantly exists in its molecular and positively charged ionic forms when the pH is between 3.0 and 7.0. The ionic form of aniline interacts with MB500 through electrostatic effects. However, as the pH increases, the proportion of ionic aniline decreases, weakening its electrostatic interaction with MB500. Even within the pH range of 7.0 to 10.0, some removal of aniline in its molecular form was observed, suggesting that additional adsorption mechanisms, beyond electrostatic interactions, contribute to the adsorption of aniline by MB500.

Other mechanisms, such as hydrogen bonds, π–π interactions, and hydrophobic interactions, also contribute to the adsorption of aniline, as confirmed by the FTIR and XPS spectra analyses. Figure 8a displays the FTIR spectra of MB500 before and after aniline adsorption. The spectra revealed that the peak at 3385 cm^{-1}, corresponding to the stretching vibrations of –OH groups and N–H bonds, became broader and more intense following adsorption. This alteration suggests that aniline was adsorbed onto MB500 through hydrogen bonding between the $–NH_2$ groups of aniline and the –OH groups on the MB500 surface (Yu et al. 2017). Small shifts and increased intensities of the peak at 1590 cm^{-1}, corresponding to stretching vibration of aromatic ring skeleton or N–H bending vibration in aniline, suggest π–π interactions between the benzene ring of aniline and the electron-depleted areas of MB500 (Yu et al. 2016, 2024). The increased intensity of the peak at 1222 cm^{-1}, which is associated with both C–N stretching and ring stretching vibrations (Suresh et al. 2013; Yu et al. 2017), confirms the binding of aniline to the surface of MB500 during the interaction process. Further, due to π–π interactions (Zhang et al. 2022a, b), the peaks between 600 and 900 cm^{-1}, associated with the out-of-plan bending of aromatic carbon (Yu et al. 2018), became more pronounced following aniline adsorption. These observations collectively suggest that both hydrogen bonding and π-π interactions play significant roles in the adsorption of aniline onto MB500.

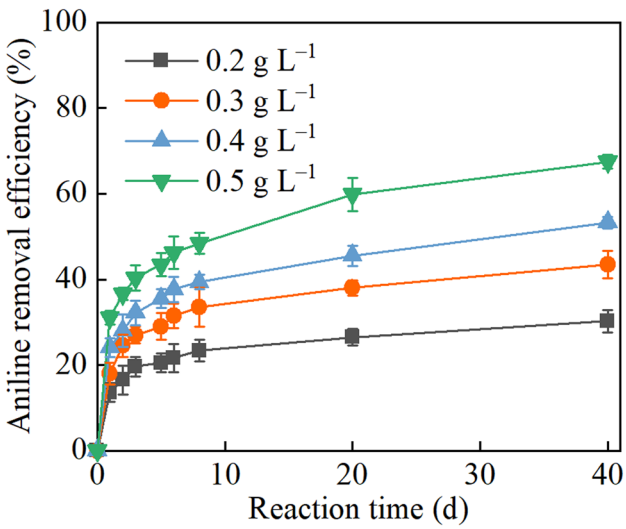

Fig. 7 Adsorption based removal of aniline by MB500 over various periods (initial pH = 7, aniline concentration = 10 mg L^{-1})

The XPS spectra before and after aniline adsorption are presented in Fig. 8b–d. After aniline adsorption, the content of O and N elements on the surface of MB500 decreased while the content of C increased, indicating a reduction in the hydrophilicity of MB500. Aniline contains hydrophobic groups (i.e., phenyl groups), which can interact with the benzene rings of aromatic acids through hydrophobic effects and π–π bonding (Yu et al. 2017). Furthermore the high-resolution C1s and O1s spectra revealed an increase in the relative intensities of the C–C and π–π satellite peaks, providing further evidence of aniline adsorption on the MB500 surface and the involvement of π-π interactions. The adsorption of aniline also caused a reduction in the relative abundance of C=C, C=O, and O–C=O groups. This suggests that hydrogen bonding may have altered the electrochemical environment of the biochar surface, leading to an increased formation of C–O groups (Yu et al. 2017). The high-resolution N 1 s spectra showed that after aniline adsorption, the content of pyridinic N decreased from 43.41 to 39.57%, and its peak shifted to lower binding energy. This shift is primarily due to changes in the electron density around the nitrogen atom caused by electron transfer from pyridinic N to aniline. These experimental findings, along with the results from PFRs generation and long-term adsorption tests, further support the idea that pyridinic N within PFRs may participate in direct redox reactions with aniline (Wu et al. 2021), contributing to the partial degradation of the contaminant.

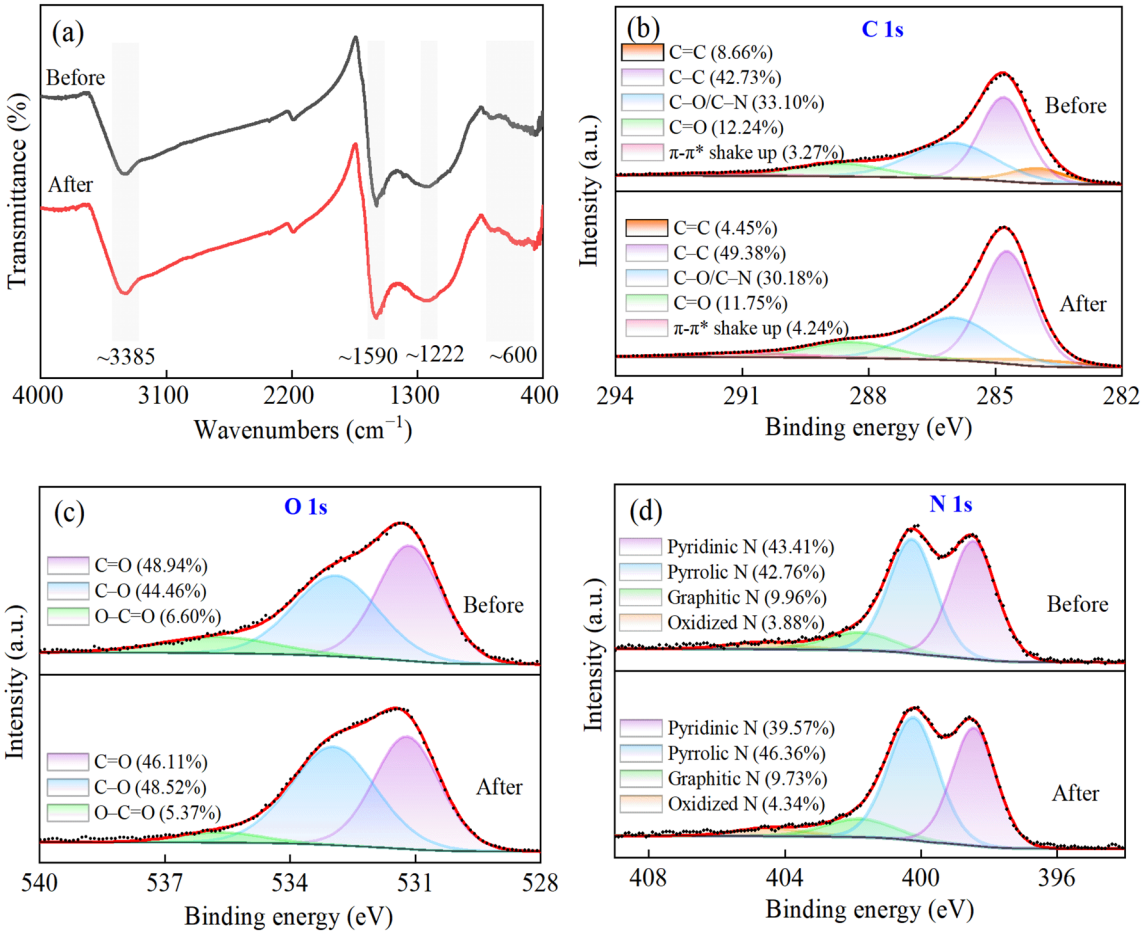

Fig. 8 FTIR spectra (**a**) and high-resolution C 1 s (**b**), O1s, and N1s (**c**) XPS spectra of MB500 before and after aniline adsorption

3.5 Reactive species formation in MB500/PMS system

To identify the primary reactive species generated during PMS activation, chemical quenching experiments were conducted. Figure 9 illustrates the effects of various scavengers, namely MeOH, TBA, *p*-BQ, FFA, and KI, on aniline removal by the MB500/PMS catalytic system. The introduction of TBA and MeOH at concentrations of 5 and 10 mmol L^{-1} did not significantly suppress aniline removal, particularly in the case of TBA, indicating that ·OH and $SO_4^{\cdot-}$ were not the dominant reactive species in this system. However, the presence of *p*-BQ and FFA at 5 mmol L^{-1} significantly inhibited aniline degradation, reducing the removal efficiency by 24% and 17%, respectively. This inhibition was further enhanced at a concentration of 10 mmol L^{-1}. These results suggest that $O_2{\cdot}^-$ generated in the MB500/PMS catalytic system plays a crucial role in aniline degradation, followed by $^1O_2$, while $SO_4^{\cdot-}$ and ·OH have lesser contributions. The addition of KI, which primarily detects surface-bound reactive species, resulted in a moderate inhibition in aniline removal, decreasing the removal efficiency by 21% at a concentration of 10 mmol L^{-1}. This indicates that the catalytic oxidation reaction occurred both in the bulk solution and at the catalyst interface, with respective contributions of approximately 70% and 30%. Based on these results, it can be concluded that radical reactions, along with non-radical pathways occurring mainly in the bulk solution, were responsible for the aniline removal in the MB500/PMS catalytic system.

The reactive species generated by the MB500/PMS system were further investigated using the EPR analysis, employing DMPO and TEMP as spin-trapping reagents. As shown in Fig. S12, no significant EPR signals were detected with MB500 alone. However, in MB500/PMS catalytic system, characteristic signals for DMPO and TEMP spin trappig adducts were observed, confirming the generation of ·OH, $SO_4^{\cdot-}$, $O_2^{\cdot-}$, and $^1O_2$ during the reaction. The intensities of these EPR signals increased with the extension of reaction time (Fig. S13), with the concentration of each reactive species reaching 4.21×10^{11} spins mm^{-3}, 5.93×10^{11} spins mm^{-3}, 1.72×10^{13} spins mm^{-3}, 7.13×10^{11} spins mm^{-3}

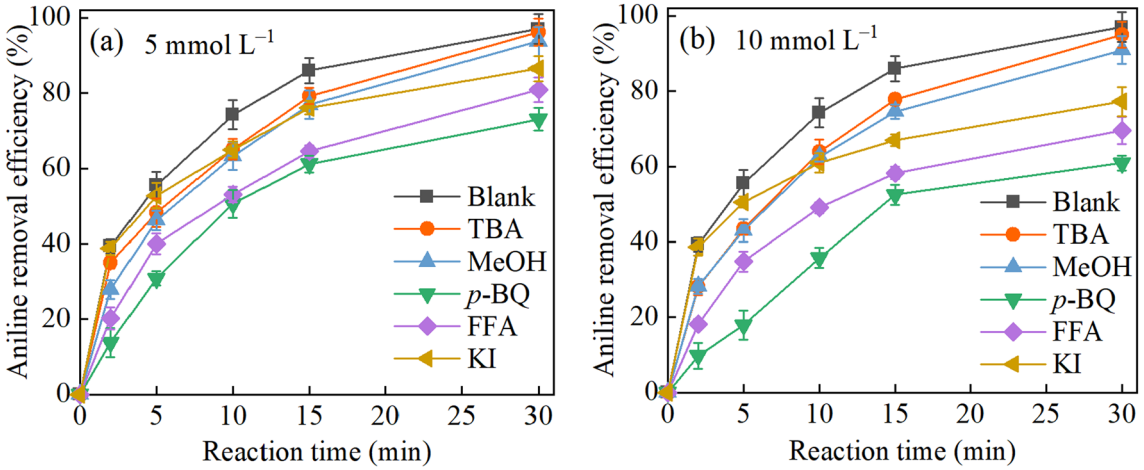

Fig. 9 Effect of scavenger types and concentrations on aniline removal by the MB500/PMS catalytic system (initial pH = 7, aniline concentration = 10 mg L^{-1}, PMS concentration = 0.2 g L^{-1}, MB500 dosage = 0.7 g L^{-1})

at 30 min, respectively. To determine the correlation among the amount of PFRs, formation of reactive species, and efficiency of aniline removal, linear fitting was performed. As shown in Fig. 10a and Table 1, there was a highly negative correlation between the generation of $SO_4^{\cdot-}$ and $O_2^{\cdot-}$ and the concentration of biochar-PFRs ($R^2 = 0.908$ and 0.897, respectively). However, the linear correlation coefficient between PFRs concentration and the generation of ·OH and $^1O_2$ was weak, indicating that the PFRs were the main contributors to the formation of $SO_4^{\cdot-}$ and $O_2^{\cdot-}$. This finding differs from previous studies, where $SO_4^{\cdot-}$ and ·OH were typically considered the main reactive radicals in catalytic PMS activation (Yu et al. 2020). Therefore, it is entirely feasible to control the formation of reactive species in biochar-catalyzed advanced oxidation processes through surface modification via Na_2CO_3 activation and hetero-atom N doping. According to previous research, biochar-PFRs can directly transfer a single electron to PMS molecules and adsorbed molecular oxygen, resulting in the formation of $SO_4^{\cdot-}$ and $O_2^{\cdot-}$ (Liu et al. 2024a, b; Luo et al. 2021; Zhang et al. 2023; Zhao et al. 2021), respectively (Eqs. 1 and 2). $O_2^{\cdot-}$ can react with PMS molecules or disproportionate to H_2O_2, further generating $SO_4^{\cdot-}$ and ·OH (Yu et al. 2020). Partially generated $SO_4^{\cdot-}$ from these pathways then reacts with H_2O or OH^- to form ·OH (Wu et al. 2021; Yu et al. 2020) (Eqs. 3 and 4). To confirm the role of adsorbed molecular oxygen in aniline removal, dissolved oxygen (DO) in the reaction was removed by N_2 pre-sparging. Unexpectedly, no significant difference in aniline removal efficiency was observed with or without DO (Fig. S14). This indicates that the adsorbed molecular oxygen did not contribute as a source of $O_2^{\cdot-}$ in the presence of biochar-PFRs. In fact, various PFRs could react with H_2O to generate $HO_2\cdot$ by one-electron transfer (Eq. (5)) (Luo et al. 2021), which can be subsequently converted to $O_2^{\cdot-}$ under alkaline conditions. Previous studies have confirmed that $O_2^{\cdot-}$ is easily converted into $^1O_2$ within the degradation system (Eqs. 6–8). However, due to the poor correlation between PFRs and $^1O_2$ generation in this study, it can be inferred that other pathways for $^1O_2$ generation might exist that are not affected by $O_2^{\cdot-}$. The electrophilic addition and electron abstraction on the surface of biochar-based catalysts are the key chemical processes taking place in the $^1O_2$ dominated non-radical pathways (Liu et al. 2023). In this study, the ketone structure in biochar at the edge of the carbon matrix (Luo et al. 2021) may serve as an electron acceptor to induce PMS to produce $^1O_2$ through a series of reactions, such as additive reactions, dehydration, and ring-opening reactions (Hu et al. 2020; Qi et al. 2020). Due to its higher electronegativity compared to carbon, the graphitic N doped into the sp^2-hybridized carbon ring withdraws electrons from neighboring carbon atoms, resulting in a positive charge on the adjacent carbon atoms. This electron-deficient carbon atom then attracts electrons from PMS, facilitating the formation of $SO_5\cdot^-$ through a nucleophilic addition reaction. This species can further react with water to generate $^1O_2$ (Eqs. 9 and 10) (Liu et al. 2023; Zhao et al. 2021). $^1O_2$ can also be produced through PMS self-decomposition (Eq. (11)) (Liu et al. 2023; Zhao et al. 2021), and the coexistence of ·OH, $SO_4^{\cdot-}$, and $O_2^{\cdot-}$ in the reaction system can also lead to the production of $^1O_2$ (Eqs. 12–14) (Huang et al. 2021).

$$HSO_5^- + e_{BC}^- \rightarrow SO_4^{\cdot-} + OH^- \quad (1)$$

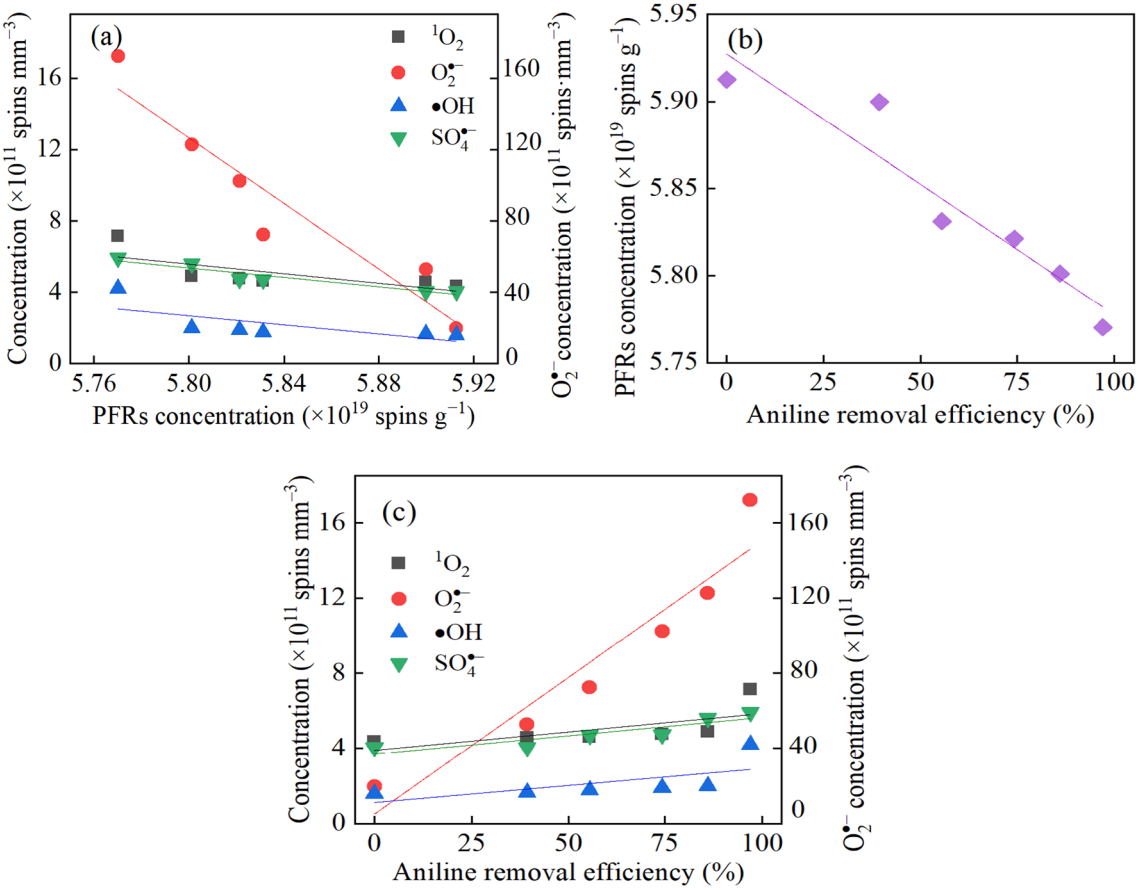

Fig. 10 Correlation analysis of PFRs concentrations, reactive specie formation, and aniline removal efficiency

Table 1 Linear fitting of the relationship between PFRs concentration and reactive species concentration during the reaction

Reactive species types	Fitting curve equation	Correlation coefficient R^2
·OH	y = −15.87x + 97.59	0.505
$SO_4^{\cdot-}$	y = −14.35x + 88.80	0.897
$O_2^{\cdot-}$	y = −92.02x + 546.38	0.908
$^1O_2$	y = −13.41x + 83.38	0.525

$$O_2 + e_{BC}^- \rightarrow O_2^{\cdot-} \quad (2)$$

$$SO_4^{\cdot-} + OH^- \rightarrow \cdot OH + SO_4^{2-} \quad (3)$$

$$SO_4^{\cdot-} + H_2O \rightarrow \cdot OH + SO_4^{2-} + H^+ \quad (4)$$

$$PFRs + H_2O \rightarrow HO_2\cdot \quad (5)$$

$$2O_2^{\cdot-} + 2H_2O \rightarrow H_2O_2 + {}^1O_2 + 2OH^- \quad (6)$$

$$2O_2^{\cdot-} + 2H^+ \rightarrow {}^1O_2 + H_2O_2 \quad (7)$$

$$O_2^{\cdot-} + \cdot OH \rightarrow {}^1O_2 + OH^- \quad (8)$$

$$HSO_5^- \rightarrow SO_5\cdot^- + H^+ + e^- \quad (9)$$

$$4SO_5\cdot^- + 2H_2O \rightarrow 4HSO_4^- + {}^1O_2 \quad (10)$$

$$HSO_5^- + SO_5^{2-} \rightarrow SO_4^{2-} + HSO_4^- + {}^1O_2 \quad (11)$$

$$O_2^{\cdot-} + \cdot OH \rightarrow {}^1O_2 + OH^- \quad (12)$$

$$SO_4^{\cdot-} + O_2^{\cdot-} \rightarrow SO_4^{2-} + {}^1O_2 \quad (13)$$

$$2O_2^{\cdot-} + 2H^+ \rightarrow {}^1O_2 + H_2O_2 \quad (14)$$

In order to gain an in-depth understanding of the contribution of PFRs to pollutant removal, the relationships between biochar properties, PFRs concentration, generated reactive species, and aniline degradation were further explored. As shown in Fig. 10b and Table 2, a strong linear correlation existed between the removal efficiency of aniline and the concentrations of $SO_4^{\cdot-}$, $O_2^{\cdot-}$, and PFRs were relatively high, with R^2 values of 0.787, 0.908, and 0.901, respectively. Correlations with other reactive species were weak. When combined with the quenching experiments and DMPO adducts, these results suggest that PFRs play a significant role in aniline removal. They primarily induce the production of $O_2^{\cdot-}$ and $SO_4^{\cdot-}$, with $O_2^{\cdot-}$ being the key species for contaminant degradation. Not only does $O_2^{\cdot-}$ act as the primary species for the oxidative degradation of aniline, but it also indirectly participates in oxidation of aniline by acting as an intermediate species for the generation of $^1O_2$, which further contributes to aniline degradation.

Table 2 Linear fitting of the relationship among PFRs concentration, reactive species concentration, and aniline removal efficiency during the reaction

Reactive species types	Fitting curve equation	Correlation coefficient R^2
·OH	$y = -0.018x + 1.12$	0.412
$SO_4^{\cdot-}$	$y = -0.019x + 3.70$	0.787
$O_2^{\cdot-}$	$y = -0.15x + 0.51$	0.908
$^1O_2$	$y = -0.020x + 3.90$	0.447
PFRs	$y = -0.0015x + 5.93$	0.901

3.6 Reaction mechanism analysis

Based on the above discussion, the possible mechanism of PMS activation by biochar-PFRs for aniline removal was proposed and is illustrated in Fig. 11. The collaborative modification of urea and Na_2CO_3 creates more pyridinic N heterocyclic defects in mesoporous biochar. These defects facilitate the formation of C=O functional groups and C=C bonds, redistributing excess electrons to the adjacent sp2-hybridized carbon atoms in the carbon-based framework via the delocalized π-conjugated network (Zhang et al. 2022a, b). This electron transfer alters the original state of PFRs on the biochar surface, particularly their concentration, resulting in the formation of more oxygen- and carbon-centered PFRs at 500 °C.

Given the relatively small specific surface area and pore volume of the modified biochar at this temperature,

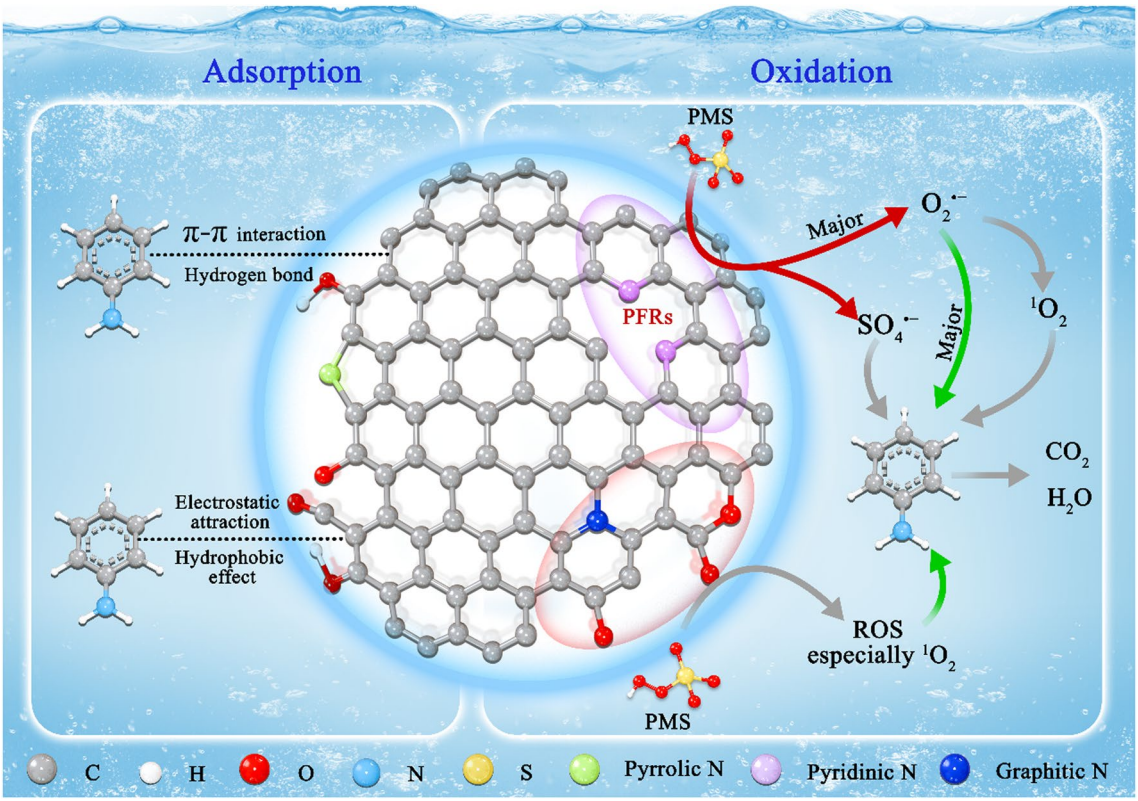

Fig. 11 Proposed mechanism of PMS activation by biochar-PFRs for aniline removal

during the catalytic oxidation reaction, aniline molecules predominantly interacted with active sites such as pyridinic N and graphitic N on the biochar surface. These interactions occurred through various chemical mechanisms, including electrostatic interactions, hydrogen bonding, π–π interactions, and hydrophobic effects. The bonded aniline molecules were then oxidized via a direct electron-transfer mechanism by PFRs, with the process potentially extending over a prolonged reaction time of up to 40 days (Zhao et al. 2021). However, this direct oxidation process is negligible within the 30 min timeframe of this study. In the indirect oxidation process, the single-electron transfer from various active sites, such as sp^2 C=C, and pyridinic N of PFRs in biochar, reacts with H_2O and PMS, leading to the generation of various reactive species, particularly $O_2^{\cdot-}$ and $SO_4^{\cdot-}$. All of these produced reactive species contribute to aniline removal, with the $O_2^{\cdot-}$ radical pathway being the most effective, outperforming the $^1O_2$, $SO_4^{\cdot-}$ and ·OH in the MB500/PMS system. In this process, organic contaminants lose electrons, converting into intermediate products or being directly mineralized into CO_2 and H_2O (Zhao et al. 2021). The reasons behind the dominant role of $O_2^{\cdot-}$ and the dynamic relationship with the species in biochar-based catalysts require further exploration in future studies. As active sites such as C=C, C=O, O–C=O, pyridinic N, and graphitic N are lost, along with a reduction in catalytic activity, the efficiency of aniline removal gradually decreases with each use.

4 Conclusions

In this study, biochar enriched with PFRs was synthesized through a combined modification process involving urea and Na_2CO_3. The factors influencing PFR formation were investigated, demonstrating that C=C bonds, the I_D/I_G ratio, and pyridinic N are key determinants in the generation of PFRs. Batch experiments showed that, under neutral conditions, the MB500/PMS catalytic system achieved a 92% removal rate of aniline within 30 min and demonstrated excellent tolerance to anions. It was found that aniline removal occurs through two primary mechanisms: direct oxidation by PFRs and indirect oxidation via active species generated by PFR activation, particularly $O_2^{\cdot-}$. This study provides new insights into the synergistic effects of combined modifications on PFR formation in biochar, laying a solid theoretical foundation for the structural design and functional optimization of biochar. Furthermore, it presents an innovative approach for the effective removal of recalcitrant pollutants from water, positioning biochar as a highly promising candidate for large-scale wastewater treatment. Reflecting on limitations of the study, future research should focus on the application of PFR-enriched biochar for treating diverse real-world wastewater, the full utilization of various active sites on the biochar surface to enhance its efficacy, and the development of effective regeneration techniques to enable efficient recycling. These advancements will support the broader application of biochar in environmental remediation.

Supplementary Information

The online version contains supplementary material available at https://doi.org/10.1007/s42773-024-00416-0.

Supplementary Material 1.

Acknowledgements
We appreciate the General Program of Stable Support Plan for Universities in Shenzhen City (Grant No. GXWD20231130102759003) and the National Natural Science Foundation of China (Grant No. 42177044) for funding.

Author contributions
Zilong Zhao: conceptualization, methodology, data curation, writing—original draft, writing—review and editing, supervision, project administration, funding acquisition, resources. Shuting Zhu: methodology, validation, data curation, visualization. Shuyu Qi: methodology, writing—original draft, writing—review and editing. Ting Zhou: software, methodology, data curation. Yang Yang: software, data curation. Feng Wang: software, data curation. Qi Han: software, data curation. Wenyi Dong: supervision, resources. Hongjie Wang: resources. Feiyun Sun: resources.

Funding
This research was fouded by the General Program of Stable Support Plan for Universities in Shenzhen City (Grant No. GXWD20231130102759003) and the National Natural Science Foundation of China (Grant No. 42177044).

Availability of data and materials
The data that support this study are available from the corresponding author upon reasonable request.

Declarations

Competing interests
The authors declare that they have no known competing financial interests or personal relationships that could have appeared to influence the work reported in this paper.

Author details
[1]School of Civil and Environmental Engineering, Harbin Institute of Technology Shenzhen, Xili University Town, Nanshan District, Shenzhen 518055, People's Republic of China. [2]Low-Carbon and Ecological Environmental Protection Research Center, Chongqing Academy of Science and Technology, Chongqing 401120, People's Republic of China. [3]Shenzhen Key Laboratory of Water Resource Utilization and Environmental Pollution Control, Shenzhen 518055, People's Republic of China. [4]State Key Laboratory of Urban Water Resource and Environment, School of Environment, Harbin Institute of Technology, Harbin 150090, People's Republic of China. [5]Joint Laboratory of Urban High Strength Wastewater Treatment and Resource Utilization, Harbin Institute of Technology (Shenzhen), Shenzhen 518055, People's Republic of China.

Received: 16 July 2024 Revised: 6 December 2024 Accepted: 12 December 2024
Published online: 29 January 2025

References

Bi D, Huang F, Jiang M, He Z, Lin X (2022) Effect of pyrolysis conditions on environmentally persistent free radicals (EPFRs) in biochar from co-pyrolysis of urea and cellulose. Sci Total Environ 805:150339. https://doi.org/10.1016/j.scitotenv.2021.150339

Chen D, Xu J, Ling P, Fang Z, Re Q, Xu K, Jiang L, Wang Y, Su S, Hu S, Xiang J (2024) Formation and evolution mechanism of persistent free radicals in biochar during biomass pyrolysis: Insights from biochar's element composition and chemical structure. Fuel 357:129910. https://doi.org/10.1016/j.fuel.2023.129910

Ding D, Yang S, Qian X, Chen L, Cai T (2020) Nitrogen-doping positively whilst sulfur-doping negatively affect the catalytic activity of biochar for the degradation of organic contaminant. Appl Catal B: Environ 263:118348. https://doi.org/10.1016/j.apcatb.2019.118348

Hu W, Tan J, Pan G, Chen J, Chen Y, Xie Y, Wang Y, Zhang Y (2020) Direct conversion of wet sewage sludge to carbon catalyst for sulfamethoxazole degradation through peroxymonosulfate activation. Sci Total Environ 728:138853. https://doi.org/10.1016/j.scitotenv.2020.138853

Hu S, Liu C, Bu H, Chen M, Fei Y (2024) Efficient reduction and adsorption of Cr(VI) using $FeCl_3$ -modified biochar: synergistic roles of persistent free radicals and Fe(II). J Environ Sci 137:626–638. https://doi.org/10.1016/j.jes.2023.03.011

Huang W, Xiao S, Zhong H, Yan M, Yang X (2021) Activation of persulfates by carbonaceous materials: a review. Chem Eng J 418:129297. https://doi.org/10.1016/j.cej.2021.129297

Huang F, Bi D, Liu S, Yi W, Zhang J, Yao D (2022) Formation and regulation of environmentally persistent free radicals in biochar and removal of diethyl-phthalate in water. J Anal Appl Pyrolysis 168:105770. https://doi.org/10.1016/j.jaap.2022.105770

Li D, Duan X, Sun H, Kang J, Zhang H, Tade M, Wang S (2017) Facile synthesis of nitrogen-doped graphene via low-temperature pyrolysis: the effects of precursors and annealing ambience on metal-free catalytic oxidation. Carbon 115:649–658. https://doi.org/10.1016/j.carbon.2017.01.058

Lin X, Chen X, Fu P, Tang B, Bi D (2023) Highly efficient production of monocyclic aromatics from catalytic co-pyrolysis of biomass and plastic with nitrogen-doped activated carbon catalyst. Chem Eng J 474:145783. https://doi.org/10.1016/j.cej.2023.145783

Liu B, Guo W, Wang H, Si Q, Zhao Q, Luo H, Ren N (2020) Activation of peroxymonosulfate by cobalt-impregnated biochar for atrazine degradation: the pivotal roles of persistent free radicals and ecotoxicity assessment. J Hazard Mater 398:122768. https://doi.org/10.1016/j.jhazmat.2020.122768

Liu T, Cui K, Li C-X, Chen Y, Wang Q, Yuan X, Chen Y, Liu J, Zhang Q (2023) Efficient peroxymonosulfate activation by biochar-based nanohybrids for the degradation of pharmaceutical and personal care products in aquatic environments. Chemosphere 311:137084. https://doi.org/10.1016/j.chemosphere.2022.137084

Liu F, Ding J, Zhao Q, Zhao G, Wang K, Li L, Guan S (2024a) Insight into the self-driven O_2 activation and interfacial electron transfer for micropollutant degradation by boron-doped biochar: role of boron moieties and persistent free radicals. Sep Purif Technol 330:125444. https://doi.org/10.1016/j.seppur.2023.125444

Liu X, Chen Z, Lu S, Shi X, Qu F, Cheng D, Wei W, Shon H-K, Ni B-J (2024b) Persistent free radicals on biochar for its catalytic capability: a review. Water Res 250:120999. https://doi.org/10.1016/j.watres.2023.120999

Luo K, Yang Q, Pang Y, Wang D, Li X, Lei M, Huang Q (2019) Unveiling the mechanism of biochar-activated hydrogen peroxide on the degradation of ciprofloxacin. Chem Eng J 374:520–530. https://doi.org/10.1016/j.cej.2019.05.204

Luo K, Pang Y, Wang D, Li X, Wang L, Lei M, Huang Q, Yang Q (2021) A critical review on the application of biochar in environmental pollution remediation: role of persistent free radicals (PFRs). J Environ Sci 108:201–216. https://doi.org/10.1016/j.jes.2021.02.021

Qi Y, Ge B, Zhang Y, Jiang B, Wang C, Akram M, Xu X (2020) Three-dimensional porous graphene-like biochar derived from *Enteromorpha* as a persulfate activator for sulfamethoxazole degradation: role of graphitic N and radicals transformation. J Hazard Mater 399:123039. https://doi.org/10.1016/j.jhazmat.2020.123039

Ruan X, Sun Y, Du W, Tang Y, Liu Q, Zhang Z, Doherty W, Frost R, Qian G, Tsang D (2019) Formation, characteristics, and applications of environmentally persistent free radicals in biochars: a review. Bioresour Technol 281:457–468. https://doi.org/10.1016/j.biortech.2019.02.105

Suresh S, Srivastava VC, Mishra IM (2013) Studies of adsorption kinetics and regeneration of aniline, phenol, 4-chlorophenol and 4-nitrophenol by activated carbon. Chem Ind Chem Eng Q 19(2):195–212. https://doi.org/10.2298/CICEQ111225054S

Tao W, Duan W, Liu C, Zhu D, Si X, Zhu R, Oleszczuk P, Pan B (2020) Formation of persistent free radicals in biochar derived from rice straw based on a detailed analysis of pyrolysis kinetics. Sci Total Environ 715:136575. https://doi.org/10.1016/j.scitotenv.2020.136575

Tao W, Zhang P, Li H, Yang Q, Oleszczuk P, Pan B (2022) Generation mechanism of persistent free radicals in lignocellulose-derived biochar: roles of reducible carbonyls. Environ Sci Technol 56:10638–10645. https://doi.org/10.1021/acs.est.1c06997

Wen Y, Liu L, He D, Wu J, Yang W, Li S, Wang S, Shu L, Zhou Z, Zhou Z, Zhou N (2024) Highly graphitized biochar as nonmetallic catalyst to activate peroxymonosulfate for persistent quinclorac removal in soil through both free and non-free radical pathways. Chem Eng J 480:148082. https://doi.org/10.1016/j.cej.2023.148082

Wu W, Zhu S, Huang X, Wei W, Jin C, Ni B-J (2021) Determination of instinct components of biomass on the generation of persistent free radicals (PFRs) as critical redox sites in pyrogenic chars for persulfate activation. Environ Sci Technol 55:7690–7701. https://doi.org/10.1021/acs.est.1c01882

Xie J, Latif J, Yang K, Wang Z, Zhu L, Yang H, Qin J, Ni Z, Jia H, Xin W, Li X (2024) A state-of-art review on the redox activity of persistent free radicals in biochar. Water Res 255:121516. https://doi.org/10.1016/j.watres.2024.121516

Yan Y, Ma X, Cao W, Zhang X, Zhou J, Liu Q, Qian G (2018) Identifying the reducing capacity of biomass derived hydrochar with different post-treatment methods. Sci Total Environ 643:486–495. https://doi.org/10.1016/j.scitotenv.2018.06.232

Yang J, Pan B, Li H, Liao S, Zhang D, Wu M, Xing B (2016) Degradation of *p*-nitrophenol on biochars: role of persistent free radicals. Environ Sci Technol 50:694–700. https://doi.org/10.1021/acs.est.5b04042

Yu S, Wang X, Ai Y, Tan X, Hayat T, Hu W, Wang X (2016) Experimental and theoretical studies on competitive adsorption of aromatic compounds on reduced graphene oxides. J Mater Chem A 4:5654–5662. https://doi.org/10.1039/C6TA00890A

Yu S, Wang X, Chen Z, Wang J, Wang S, Hayat T, Wang X (2017) Layered double hydroxide intercalated with aromatic acid anions for the efficient capture of aniline from aqueous solution. J Hazard Mater 321:111–120. https://doi.org/10.1016/j.jhazmat.2016.09.009

Yu W, Lian F, Cui G, Liu Z (2018) N-doping effectively enhances the adsorption capacity of biochar for heavy metal ions from aqueous solution. Chemosphere 193:8–16. https://doi.org/10.1016/j.chemosphere.2017.10.134

Yu J, Zhu Z, Zhang H, Shen X, Qiu Y, Yin D, Wang S (2020) Persistent free radicals on N-doped hydrochar for degradation of endocrine disrupting compounds. Chem Eng J 398:125538. https://doi.org/10.1016/j.cej.2020.125538

Yu C, Xing J, Xu K, Chen S (2024) Enhanced adsorption of micropollutants on oxygen plasma-modified carbon nanotubes (O-CNTs) under electrochemical assistance. J Water Process Eng 58:104854. https://doi.org/10.1016/j.jwpe.2024.104854

Yuan J, Wen Y, Dionysiou DD, Sharma VK, Ma X (2022) Biochar as a novel carbon-negative electron source and mediator: electron exchange capacity (EEC) and environmentally persistent free radicals (EPFRs): a review. Chem Eng J 429:132313. https://doi.org/10.1016/j.cej.2021.132313

Zhang Y, Xu M, He R, Zhao J, Kang W, Lv J (2022a) Effect of pyrolysis temperature on the activated permonosulfate degradation of antibiotics in nitrogen and sulfur-doping biochar: key role of environmentally persistent free radicals. Chemosphere 294:133737. https://doi.org/10.1016/j.chemosphere.2022.133737

Zhang Z, Yang R, Zheng Y, Bai H, Shi J, Zhang J, Zhou X, Cai M, Fan S, Li C (2022b) Graphene oxide-Fe_3O_4 nanocomposite used as aniline adsorbent with a wide pH range. Colloid Polym Sci 300:83–93. https://doi.org/10.1007/s00396-021-04926-2

Zhang R, Zhang R, Zimmerman A, Wang H, Gao B (2023) Applications, impacts, and management of biochar persistent free radicals: a review. Environ Pollut 327:121543. https://doi.org/10.1016/j.envpol.2023.121543

Zhang J, Liu S, Huang F, Bi D, Song J, Chou S (2024) Coupled effects of Fenton-like systems with different concentrations of H_2O_2/Biochar on diethyl phthalate removal: dominant role of environmental persistent

free radicals (EPFRs). Environ Pollut 385:124499. https://doi.org/10.1016/j.envpol.2024.124499

Zhao C, Shao B, Yan M, Liu Z, Liang Q, He Q, Wu T, Liu Y, Pan Y, Huang J, Wang J, Liang J, Tang L (2021) Activation of peroxymonosulfate by biochar-based catalysts and applications in the degradation of organic contaminants: a review. Chem Eng J 416:128829. https://doi.org/10.1016/j.cej.2021.128829

Zhu S, Huang X, Ma F, Wang L, Duan X, Wang S (2018) Catalytic removal of aqueous contaminants on N-doped graphitic biochars: inherent roles of adsorption and nonradical mechanisms. Environ Sci Technol 52:8649–8658. https://doi.org/10.1021/acs.est.8b01817

Zhu S, Huang X, Yang X, Peng P, Li Z, Jin C (2020) Enhanced transformation of Cr(VI) by heterocyclic-N within nitrogen-doped biochar: impact of surface modulatory persistent free radicals (PFRs). Environ Sci Technol 54:8123–8132. https://doi.org/10.1021/acs.est.0c02713

Zhu Y, Wei J, Li J (2023) Biochar-activated persulfate oxidation of arsenic(III): nonnegligible roles of environmentally persistent free radicals. J Environ Chem Eng 11:111033. https://doi.org/10.1016/j.jece.2023.111033